

Thermoelectric properties of superlattice nanowires

Yu-Ming Lin

Department of Electrical Engineering and Computer Science, Massachusetts Institute of Technology, Cambridge, Massachusetts 02139-4307, USA

M. S. Dresselhaus*

Department of Physics, Department of Electrical Engineering and Computer Science, Massachusetts Institute of Technology, Cambridge, Massachusetts 02139-4307, USA

(Received 1 March 2003; published 7 August 2003)

We report here on a theoretical model for the electronic structure and transport properties of superlattice nanowires, considering their cylindrical wire boundary and multiple anisotropic carrier pockets. The thermoelectric properties of superlattice nanowires made of various lead salts (PbS, PbSe, and PbTe) are investigated as a function of the segment length, wire diameter, crystal orientation along the wire axis, and the length ratio of the constituent nanodots of the superlattice, based on the Kronig-Penney potential for each one-dimensional (1D) subband and on the 1D Boltzmann transport equations. A potential barrier-well inversion induced by quantum confinement, which is a unique phenomenon in superlattice nanowires, is predicted as the wire diameter decreases. ZT values higher than 4 and 6 are predicted for 5-nm-diameter PbSe/PbS and PbTe/PbSe superlattice nanowires at 77 K, respectively. These ZT values are significantly larger than those of their corresponding alloy nanowires, indicating that superlattice nanowires are promising systems for thermoelectric applications.

DOI: 10.1103/PhysRevB.68.075304

PACS number(s): 73.63.Kv, 72.15.Jf

I. INTRODUCTION

Studies on low-dimensional systems, such as one-dimensional (1D) quantum wires and 2D superlattices, have attracted considerable attention, spurred on by the urge to develop smaller and faster electronic devices and by the hope to exploit their unusual properties for improved performance in various applications, such as optics,^{1,2} microelectronics,³ thermoelectrics,⁴⁻⁶ and magnetics.⁷ Due to the large surface-to-volume ratio for enhanced surface effects and possible quantum confinement effects, these nanostructured materials are expected, and in some cases have been demonstrated, to exhibit dramatically different behaviors that are absent in their bulk counterparts, and can benefit certain applications. For example, Hicks and Dresselhaus^{8,9} have predicted enhanced performance for thermoelectric applications in 1D and 2D systems compared to their counterpart bulk materials, due to both a sharper density of states in low-dimensional systems for enhanced thermopower and an increased phonon scattering for reduced lattice thermal conductivity. Thermoelectric refrigeration based on nanostructures has other advantages, in addition to improved performance, in that a very small active region with a much shorter response time than those of bulk thermoelectric devices or conventional mechanical cooling systems can be achieved, which is of great interest for modern microelectronics where the efficiency bottleneck is usually limited by certain local hot spots. It is expected that by integrating nanostructured thermoelectric materials into critical regions of microelectronic circuits, the excess heat that limits the device performance can be effectively removed.

Theoretical calculations and experimental investigations of the thermoelectric properties of low dimensional 1D and 2D systems have been pursued extensively for various

materials.^{6,10,11} Since the enhancement in thermoelectric properties is anticipated to be more pronounced as the dimensionality decreases, 0D structures hold even greater promise than 1D and 2D systems. However, unlike 1D or 2D systems, where at least one of the directions is not quantum confined and thus can provide electrical conduction, 0D structures, such as quantum dots, are confined in all directions, and this may present difficulties for some applications.

To utilize the unique properties of quantum dots for situations where electron conduction is required, it is necessary to devise some means for carrier transport (e.g., tunneling or hopping) between individual dots. For this purpose, several novel structures based on quantum dots that capture the essence of 0D structures and enable transport phenomena have been proposed and synthesized, such as quantum dot array superlattices⁴ and superlattice nanowires.¹² These new structures have shown great promise in the context of thermoelectricity, and Harman *et al.* have measured an impressive thermoelectric performance of $ZT \sim 2$ at 300 K for PbTeSe-based quantum dot superlattices,⁴ compared to a highest ZT of ~ 1 for conventional bulk materials.¹¹ A possible mechanism for this enhanced thermoelectric performance has been proposed¹³ to be due to the miniband formation in coupled 3D quantum dot arrays. Other nanostructures based on quantum dots that are of great interest for thermoelectricity are superlattice nanowires (SLNW's) [see Fig. 1(a)], which consist of a series of interlaced nanodots of two different materials (denoted by A and B). In the superlattice nanowire (SLNW) structure, the electronic transport along the wire axis is made possible by the tunneling between adjacent quantum dots, while the uniqueness of each quantum dot and its 0D characteristics are maintained by the energy difference of the conduction or valence bands between different materials [see Fig. 1(b)]. The band offset not only provides some

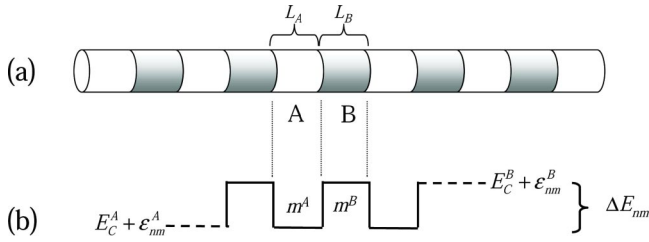


FIG. 1. (a) Schematic diagram of a superlattice nanowire consisting of interlaced nanodots *A* and *B*. (b) Schematic potential profile of one conduction subband in a superlattice nanowire.

amount of quantum confinement, but also creates a periodic potential for carriers moving along the wire axis, which may result in a sharper density of electronic states than is present in ordinary 1D systems. This new structure is especially attractive for thermoelectric applications, because the heterogeneous interfaces between the nanodots can reduce the lattice thermal conductivity by blocking the phonon conduction along the wire axis,¹⁴ while electrical conduction may be sustained and may benefit from the unusual electronic band structures due to the periodic potential perturbation. These one-dimensional heterogeneous structures also hold promise in other applications, such as nanobarcodes,¹⁵ nanolasers,¹⁶ 1D waveguides, and resonant tunneling diodes.¹⁷

Various approaches have been developed to synthesize superlattice nanowire structures with different materials. Co/Cu superlattice nanowires were first fabricated in nanoporous templates using electrochemical deposition,¹² and more recently, researchers have successfully synthesized highly crystalline semiconductor superlattice nanowires (e.g., Si/SiGe,¹⁵ GaAs/GaP,¹⁶ and InP/InAs¹⁸) by the vapor-liquid-solid growth mechanism. Due to the structural complexity and the materials diversity in these quantum dot-based systems, it is essential to develop a model to understand the behavior and to predict properties of interest in these novel structures, especially for practical applications and device optimization.

In this paper, we present a general theoretical model for the electronic structure and transport properties of superlattice nanowires, which explicitly takes into account the cylindrical wire boundary conditions, the diameter-dependent band offsets for the periodic potential along the wire axis, and the multiple anisotropic carrier pockets. The density of electronic states and the dispersion relations for each quantum subband in superlattice nanowires are presented in Sec. II using the Kronig-Penney model. With the electronic band structures thus obtained, a transport model based on the 1D Boltzmann transport equations is then developed. The effect of the superlattice structure on the phonon thermal conductivity, which is an important factor determining the thermoelectric performance, is also discussed. In Sec. III, the established transport model is utilized to study the thermoelectric properties of superlattice nanowires made of various lead salts (PbS, PbSe, and PbTe) at 77 K, which is a temperature of interest for cryogenic cooling. The lead salts are chosen for our studies of superlattice nanowires because they are conventionally good thermoelectric materials with well-established transport properties. The thermoelectric proper-

ties of these lead salt superlattice nanowires, with particular attention to PbS/PbSe systems, are investigated to elucidate their performance dependence on the segment length, wire diameter, crystal orientation along the wire axis, and the length ratio of the constituent nanodots (see Fig. 1).

II. THEORETICAL MODEL OF SUPERLATTICE NANOWIRES

A. Electronic band structure

In superlattice nanowires, their transport and other electronic properties are determined by the electronic band structure, which exhibits dramatically different features from that of a simple 1D nanowire or bulk materials. To model the electronic band structure of superlattice nanowires, we assume that each segment has a circular cross section with a uniform wire diameter d_w [see Fig. 1(a)], and the carriers in each cylindrical nanodot are confined by an infinite potential at the wire boundary (the cylindrical sidewall), which is a good approximation for nanowires embedded in a wide band gap insulating matrix or for free-standing nanowires. We also assume that each nanodot consists of a sufficient number of atoms so that the effective-mass theorem is valid to describe the local electronic properties of a nanodot by the band-structure parameters of the bulk material.

For the following discussions, the z axis is chosen to be along the wire axis, and we first consider the electronic structure in one nanodot [material *A* in Fig. 1(a), for example]. Due to the quantum confinement normal to the wire axis, quantized subbands are formed in the nanodot. These confined electrons are described by the wave function

$$\psi_{nm}^A(x, y, z) = \phi_{nm}^A(x, y) \exp(ikz), \quad (1)$$

where the superscript *A* denotes the material type, $\phi_{nm}(x, y)$ is the quantized wave function normal to the wire axis that is classified by the quantum numbers (n, m) , and k represents the electron wave vector along the wire axis (z axis). In Eq. (1), the plane wave function $\exp(ikz)$ emphasizes the unrestricted motion for electrons in the z direction within the nanodot. The energy corresponding to the electronic states of Eq. (1) is given by

$$E_{nm}^A(k) = E_C^A + \epsilon_{nm}^A + \frac{\hbar^2 k^2}{2m_z^A}, \quad (2)$$

where E_C^A is the energy of the conduction band edge for bulk material *A*, ϵ_{nm}^A is the quantization energy of the (n, m) subband, and m_z^A is the transport effective mass along the wire axis. We note that the quantization energy ϵ_{nm} and the corresponding wave function $\phi_{nm}(x, y)$ both depend on the geometry of the wire cross section, the wire diameter, and the carrier effective masses. For cylindrical 1D wires with anisotropic carrier mass tensors, the approach to calculate the wave function ϕ_{nm} and the quantized energy ϵ_{nm} has been described in Ref. 10.

By arranging the two types of nanodots (*A* and *B*) into a superlattice nanowire [see Fig. 1(a)], the electrons in the

(n, m) subband will experience a periodic square-well potential $U(z)$ with an energy barrier height

$$\Delta E_{nm} = (E_C^B + \epsilon_{nm}^B) - (E_C^A + \epsilon_{nm}^A), \quad (3)$$

when traveling along the wire axis [see Fig. 1(b)]. Although independent quantum dots possess discrete energy levels like that of atoms, superlattice nanowires exhibit 1D-like dispersion relations along the wire axis due to the wave-function leakage across the finite barrier height ΔE_{nm} between quantum dots. The (sub) band offset energies ΔE_{nm} are usually different from that of bulk materials ($E_C^A - E_C^B$) due to the quantum confinement energy ϵ_{nm} for each type of quantum dot. ΔE_{nm} may also depend on the subband index (n, m) and the wire diameter d_w .

According to the Bloch theorem,¹⁹ the eigenfunction $\eta(z)$ of the Schrodinger equation for electrons in a superlattice structure with a periodic potential $U(z)$ takes a different form from $\exp(ikz)$, and $\eta(z)$ must be of a special periodic form:

$$\eta(z+L) = \exp(i\kappa L) \eta(z), \quad (4)$$

where κ is the 1D wave vector of electrons moving along the superlattice nanowire, and $L = L_A + L_B$ is the periodic length of the superlattice nanowire. It should be pointed out that κ in Eq. (4) describes the energy-momentum relation of the *entire* superlattice nanowire, while k appearing in Eq. (1) is a property related to one nanodot only.

We note that while the electronic wave function in each nanodot is described by linear combinations of Eq. (1), the overall envelope wave function of electrons in the superlattice nanowire should be expressed as

$$\psi_{nm}(x, y, z) = \phi_{nm}(x, y) \eta(z). \quad (5)$$

The energy of electrons described by Eq. (5), which can be solved as a function of κ using the Kronig-Penney model, constitutes the important dispersion relation $E_{nm}(\kappa)$ of the (n, m) subband in the superlattice nanowire. Assuming a periodic square-well potential along the z axis, the conservation of the electron flux along the z axis is taken into account by the following boundary conditions at the interfaces:

$$\eta^A = \eta^B, \quad (6)$$

$$\frac{1}{m^A} \frac{d\eta^A}{dz} = \frac{1}{m^B} \frac{d\eta^B}{dz}. \quad (7)$$

For electrons with energies above the potential barrier ($E \geq E_C^B + \epsilon_{nm}^B$), the wave functions in each nanodot can be expressed as

$$\eta^A = a \exp(ik^A z) + b \exp(-ik^A z), \quad (8)$$

$$\eta^B = c \exp(ik^B z) + d \exp(-ik^B z), \quad (9)$$

where $a, b, c,$ and d are constants to be determined, and

$$k^A = \sqrt{2m_z^A(E - E_C^A - \epsilon_{nm}^A)}/\hbar, \quad (10)$$

$$k^B = \sqrt{2m_z^B(E - E_C^B - \epsilon_{nm}^B)}/\hbar. \quad (11)$$

By applying the boundary conditions of Eqs. (4), (6), and (7) to Eqs. (8) and (9), and eliminating the four constants ($a-d$), we obtain the following dispersion relation for κ :²⁰

$$\begin{aligned} \cos(\kappa L) &= \cos(k^A L_A) \cos(k^B L_B) - \frac{1}{2} \left(\frac{m_z^B k^A}{m_z^A k^B} + \frac{m_z^A k^B}{m_z^B k^A} \right) \\ &\times \sin(k^A L_A) \sin(k^B L_B). \end{aligned} \quad (12)$$

Similarly, for electrons with energies below the potential barrier ($E_C^A + \epsilon_{nm}^A \leq E < E_C^B + \epsilon_{nm}^B$), the wave vector κ is determined by²⁰

$$\begin{aligned} \cos(\kappa L) &= \cos(k^A L_A) \cosh(q^B L_B) - \frac{1}{2} \left(\frac{m_z^B k^A}{m_z^A q^B} + \frac{m_z^A q^B}{m_z^B k^A} \right) \\ &\times \sin(k^A L_A) \sinh(q^B L_B), \end{aligned} \quad (13)$$

where

$$q^B = \sqrt{2m_z^B(E_C^B + \epsilon_{nm}^B - E)}/\hbar. \quad (14)$$

The density of states, $D_{nm}(E)$, of the (n, m) subband is related to the energy dispersion relation by

$$D_{nm}(E) = \frac{\pi}{2} \left(\frac{\partial E_{nm}}{\partial \kappa} \right)^{-1}. \quad (15)$$

We note that, due to the periodic potential perturbation, the density of states [$D_{nm}(E)$] in a superlattice nanowire may possess a very different energy dependence from that of a simple nanowire [see Eq. (2)]. The electronic band structure [$E_{nm}(\kappa)$ and $D_{nm}(E)$] of one subband is highly dependent on the segment length L_A or L_B , the potential barrier height V_b , and the transport effective masses m_z^A and m_z^B . For example, Fig. 2 shows the density of states function $D(E)$ and the number of states $N(E) \equiv \int D(E) dE$ calculated for a subband with various segment lengths ($L_A = L_B = 1, 5, 20,$ and 60 nm), assuming a potential barrier height of $V_b = 50$ meV and an effective mass of $m_z^A = m_z^B = 0.5 m_0$, where m_0 is the free-electron mass. The zero in energy is chosen to be at the top of the potential barrier. It is found in Fig. 2(a) that for very short superlattice periods ($L_A = 1$ nm), the electronic band structure approaches that of an alloy system (alloy limit) with a density of states similar to that of a simple 1D system [see Fig. 2(a)]. In this limit, the onset of the density of states corresponds to an effective band edge in the middle of the potential well, and this effective band edge is equal to the average of the periodic potential [see Fig. 2(a)]. As the segment length increases, the density of states (or the number of states) begins to develop minibands and minigaps in the subband structure [see Figs. 2(b) and 2(c)], exhibiting features unique to the superlattice nanowires. The widths of these minibands are usually very narrow [~ 1 meV for the first miniband in Fig. 2(b)] for energies below the potential well ($E < 0$), yielding a δ function-like density of states in the potential well, as represented by vertical lines in Figs. 2(b) and 2(c), which is similar to the discrete states of quan-

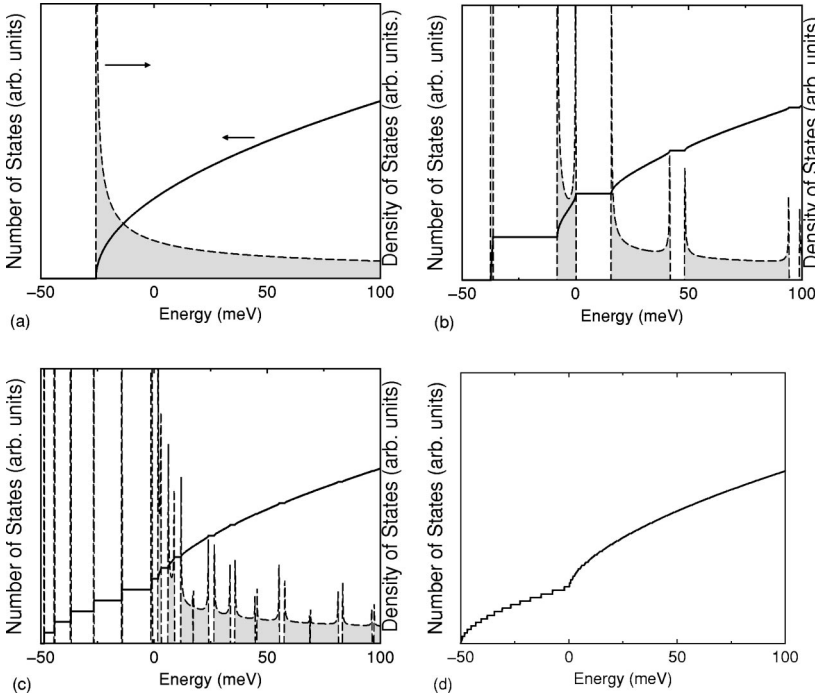


FIG. 2. Calculated density of states (---) and the number of states (—) of a 1D subband in a periodic potential with segment lengths $L_A = L_B$ of (a) 1 nm, (b) 5 nm, (c) 20 nm, and (d) 60 nm, assuming a potential barrier height of 50 meV and effective masses of $0.5m_0$. The zero in energy is chosen to be at the top of the potential barrier.

tum dots. It is found that the width of these minibands generally increases and the miniband gap decreases with increasing energy. We also note that the number of these narrow minibands in the potential well increases with increasing segment length [see Fig. 2(c)]. And for long segment lengths ($L_A \geq 60$ nm), these minibands become so close to each other in energy that they may be approximated by a continuum, if the minigaps are much smaller than the thermal energy [see Fig. 2(d)]. In this long segment length limit, the density of states of the superlattice nanowire is approximately equivalent to the averaged density of states of the two constituent materials (classical limit). In the following, we define the *alloy* and *classical* limit for superlattice nanowires that have very short and very long periods with the electronic subband structures shown in Figs. 2(a) and 2(d), respectively. It is also worth noting that in Fig. 2(c), while the minibands are well separated in energy for states with energies in the potential well ($E \leq 0$), the electronic band structure approximates the continuum of the classical limit for electrons with energies above the potential barrier ($E > 0$).

The dramatically different electronic band structures of superlattice nanowires shown in Fig. 2 can be qualitatively categorized, based on different length and energy scales: the electron de Broglie wavelength Λ_e , the segment length L_A or L_B , the mini-gap energy ϵ_g , and the thermal energy $k_B T$. In the potential well region [e.g., in the nanodot made of material A in Fig. 1(b)], the energy separation between two minibands²¹ is on the order of $\epsilon_g \sim (\pi\hbar/L)\sqrt{V_b/2m_z^A}$, and the wavelength of electrons with energy near the potential barrier is approximately $\Lambda_e \sim 2\pi\hbar/\sqrt{2m_z^A V_b}$. When the segment length is much shorter than the de Broglie wavelength Λ_e , a full electronic wavelength would cover many superlattice periods, so the electrons only experience an averaged potential without noticing the detailed potential structure as they travel along the nanowire (alloy limit). On the other

hand, if the thermal energy $k_B T$ is much larger than the minigaps ϵ_g , the minibands can be treated as continuous states due to the thermal smearing (classical limit). We define two dimensionless quantities

$$\zeta \equiv \frac{L/2}{\Lambda_e} = \frac{L\sqrt{2m_z V_b}}{4\pi\hbar} \quad (16)$$

and

$$\xi \equiv \frac{\epsilon_g}{k_B T} = \frac{\pi\hbar}{k_B T L} \sqrt{\frac{V_b}{2m_z}} \quad (17)$$

for the determination of the subband structure. The criteria for the alloy limit is then given by $L \ll \Lambda_e$ or $\zeta \ll 1$, while the condition for the classical limit is $\epsilon_g \ll k_B T$ or $\xi \ll 1$. Table I lists the calculated values of ζ and ξ corresponding to the parameters in Fig. 2 at $T = 77$ K. We note that ζ is calculated to be 0.13 for $L_A = 1$ nm [Fig. 2(a)], and ξ is 0.16 for a segment length of 60 nm [Fig. 2(d)], indicating that $\zeta \leq 0.1$ and $\xi \leq 0.1$ are satisfactory criteria for identifying the alloy limit and the classical limit, respectively, for the subband structures of superlattice nanowires. For superlattice nano-

TABLE I. Calculated ζ and ξ , defined in Eqs. (16) and (17), for determining the subband structure in a periodic potential, for various segment lengths at 77 K, assuming a potential barrier of 50 meV and an effective mass of $0.5m_0$.

Segment length ($L/2$)	1 nm (Alloy limit)	5 nm	20 nm	60 nm (Classical limit)
ζ	0.13	0.64	2.57	7.73
ξ	9.69	1.93	0.47	0.16

wires with unequal segment lengths, it is found that these conditions of ζ and ξ for the alloy and classical limits still hold for $0.1 < L_A/L_B < 10$.

B. Electrical transport properties

With the dispersion relation $E_{nm}(\kappa)$ of each subband thus obtained, important transport properties can be derived based on the Boltzmann transport equations for 1D systems.¹⁰ For simplicity, we use the constant relaxation-time approximation to calculate the following fundamental integrals for the conduction band:

$$K_{e,\alpha} = \frac{4\tau_e}{\pi^2 \hbar^2 d_w^2} \sum_{n,m} \int \frac{(E - E_F)^\alpha}{D_{nm}(E)} \left(-\frac{df}{dE} \right) dE, \quad (18)$$

where $\alpha=0,1$, or 2 , τ_e is the relaxation time for electrons, E_F is the Fermi energy, $f(E)$ is the Fermi-Dirac distribution function, and the summation is over all subbands for all electron pockets. A similar expression for holes is given by

$$K_{h,\alpha} = \frac{4\tau_h}{\pi^2 \hbar^2 d_w^2} \sum_{n,m} \int \frac{(E_F - E)^\alpha}{D_{nm}(E)} \left(-\frac{df}{dE} \right) dE. \quad (19)$$

The electrical conductivity σ , the Seebeck coefficient S , and the electrical contribution to the thermal conductivity λ_e are then obtained from K_α by

$$\sigma = e^2 (K_{e,0} + K_{h,0}), \quad (20)$$

$$S = -\frac{1}{eT} \frac{K_{e,1} - K_{h,1}}{K_{e,0} + K_{h,0}}, \quad (21)$$

$$\lambda_e = \frac{1}{T} \left(K_{e,2} + K_{h,2} - \frac{(K_{e,1} - K_{h,1})^2}{K_{e,0} + K_{h,0}} \right). \quad (22)$$

Since there is no general expression for the density of states $[D(E)]$ of superlattice nanowires, the calculation of the integrals in Eqs. (18) and (19) usually requires a considerable amount of computing resources. However, for subbands in the alloy or classical limits, the computational task can be greatly simplified by adopting analytical expressions for $D(E)$ for these two limiting conditions.

C. Lattice thermal conductivity

The phonon transport in superlattice nanowires is influenced by additional phonon scattering at the wire boundary and at the interfaces between the quantum dots. It is expected that the lattice thermal conductivity should be significantly reduced as the wire diameter or the segment length becomes smaller than the bulk phonon mean free path. The lattice thermal conductivity for superlattice nanowires has been modeled, based on the phonon Boltzmann transport equations with diffuse mismatch interface conditions.¹⁴ Assuming a diffuse nanowire boundary for phonons, which is a good approximation for nanowires with rough or imperfect surfaces, the phonon thermal conductivity λ_{SL} of superlattice nanowires is given by^{14,22}

$$\frac{L}{\lambda_{SL}} = \frac{L_A}{\lambda_A} + \frac{L_B}{\lambda_B} + 4 \left(\frac{1}{C_A v_A t_{AB}} + \frac{1}{C_B v_B t_{BA}} \right) \left(1 - \frac{t_{AB} + t_{BA}}{2} \right) + \frac{3}{d_w} \left(\frac{L_A}{C_A v_A \alpha_A} + \frac{L_B}{C_B v_B \alpha_B} \right), \quad (23)$$

where λ , C , and v are the lattice thermal conductivity, heat capacity per unit volume, and sound velocity of the bulk material (A or B), respectively. t_{AB} (or t_{BA}) is the phonon transmissivity from nanodot A to nanodot B (or B to A), which is defined as the probability of phonon energy transfer through the A - B (or B - A) interface. α_A (or α_B) is a geometric factor that only depends on the aspect ratio L_A/d_w (or L_B/d_w) of the nanodots, and it has values between 0.75 and 1 for cylindrical wires.¹⁴ In Eq. (23), the contributions of the segment interface and the wire boundary scattering processes to the lattice thermal resistivity are contained in the third and fourth terms, respectively, and the first two terms in Eq. (23) account for intrinsic phonon-scattering events present in bulk materials. Using the diffuse mismatch model^{22,23} approximation for segment interfaces, t_{AB} is given by

$$t_{AB} = \frac{C_B v_B}{C_A v_A + C_B v_B}, \quad (24)$$

and $t_{BA} = 1 - t_{AB}$. Equation (23) can then be rearranged as

$$\frac{L}{\lambda_{SL}} = \frac{L_A}{\lambda_A} \left(1 + \frac{4}{3} \frac{\Lambda_A}{L_A} + \frac{\Lambda_A}{\alpha_A d_w} \right) + \frac{L_B}{\lambda_B} \left(1 + \frac{4}{3} \frac{\Lambda_B}{L_B} + \frac{\Lambda_B}{\alpha_B d_w} \right), \quad (25)$$

where Λ_A and Λ_B are the phonon mean free paths of bulk materials A and B , respectively, which are derived from kinetic theory,

$$\lambda = \frac{1}{3} C v \Lambda. \quad (26)$$

It is convenient to define an effective phonon mean free path Λ_{eff} for one segment (A , for example) in the superlattice nanowire by

$$\Lambda_{A,\text{eff}}^{-1} = \Lambda_A^{-1} + \frac{4}{3} L_A^{-1} + \frac{1}{\alpha_A} d_w^{-1}, \quad (27)$$

and the corresponding effective thermal conductivity λ_{eff} in each segment by

$$\lambda_{A,\text{eff}} = (\Lambda_{A,\text{eff}} / \Lambda_A) \lambda_A, \quad (28)$$

which implies effective phonon-scattering lengths of $3L_A/4$ and $\alpha_A d_w$ for interface and wire boundary scattering, respectively. The lattice thermal conductivity λ_{SL} can then be concisely expressed in terms of a series of two nanodots (A and B) with effective thermal conductivities $\lambda_{A,\text{eff}}$ and $\lambda_{B,\text{eff}}$ by

$$\frac{L}{\lambda_{SL}} = \frac{L_A}{\lambda_{A,\text{eff}}} + \frac{L_B}{\lambda_{B,\text{eff}}}. \quad (29)$$

It should be noted that the derivation of Eq. (23) assumes a linear phonon dispersion relation with a constant sound velocity, which is only valid for temperatures much lower

TABLE II. The direct band gap E_g and the effective-mass components of the L -point electron and hole pockets for bulk PbS, PbSe, and PbTe, and their temperature dependence (Ref. 24).

	PbS	PbSe	PbTe
$E_g(T)$ (meV)	$263 + \sqrt{400 + 0.256T^2}$	$125 + \sqrt{400 + 0.256T^2}$	$171.5 + \sqrt{(12.8)^2 + 0.19(T+20)^2}$
$m_{e\perp}/m_0$	$\left(10.6 \frac{E_g(0)}{E_g(T)} + 1.9\right)^{-1}$	$\left(20.7 \frac{E_g(0)}{E_g(T)} + 4.3\right)^{-1}$	$\left(30.58 \frac{E_g(0)}{E_g(T)} + 14.29\right)^{-1}$
$m_{e\parallel}/m_0$	$\left(5.8 \frac{E_g(0)}{E_g(T)} + 3.7\right)^{-1}$	$\left(11.4 \frac{E_g(0)}{E_g(T)} + 2.9\right)^{-1}$	$\left(2.98 \frac{E_g(0)}{E_g(T)} + 2.42\right)^{-1}$
$m_{h\perp}/m_0$	$\left(10.6 \frac{E_g(0)}{E_g(T)} + 2.7\right)^{-1}$	$\left(20.7 \frac{E_g(0)}{E_g(T)} + 8.7\right)^{-1}$	$\left(30.58 \frac{E_g(0)}{E_g(T)} + 10.0\right)^{-1}$
$m_{h\parallel}/m_0$	$\left(5.8 \frac{E_g(0)}{E_g(T)} + 3.7\right)^{-1}$	$\left(11.4 \frac{E_g(0)}{E_g(T)} + 3.3\right)^{-1}$	$\left(2.98 \frac{E_g(0)}{E_g(T)} + 1.25\right)^{-1}$

than the Debye temperature. A more accurate description for the lattice thermal conductivity of superlattice nanowires that takes into account a nonlinear phonon dispersion relation at higher phonon frequencies can be obtained by replacing the product of the heat capacity and the sound velocity Cv in Eqs. (23)–(26) with the integration of $C(\omega)v(\omega)$ with respect to the phonon frequency ω , $\int C(\omega)v(\omega)d\omega$.

III. LEAD SALT SUPERLATTICE NANOWIRES

In this section, we apply the electronic band model and transport equations developed in Sec. II to investigate the thermoelectric properties of superlattice nanowires composed of lead salts (PbTe, PbSe, and PbS). Lead salts and their alloys are narrow-gap semiconductors that have been widely studied. They have well-established electronic properties because of their potential for tunable photoelectronic devices in the infrared and visible range.²⁴ Lead salts have also been found to be promising thermoelectric materials, going back to the early stage in thermoelectrics research, and PbS and PbTe were used in the first thermoelectric generators and cooling units, respectively.²⁵ Recently, a thermoelectric performance twice as high as the best conventional thermoelectric material has been demonstrated by lead salt quantum dot arrays,⁴ suggesting that superlattice nanowires consisting of lead salt quantum dots may also be promising thermoelectric materials.

A. Electronic band structure

The lead chalcogenide family (PbTe, PbSe, and PbS) constitutes an attractive model system to study the effect of the superlattice structure on the transport properties of nanowires, because of their simple crystal and electronic structures with well-known properties over a wide temperature range. These lead salts all possess the same NaCl-like face-centered lattice structure with lattice constants $a_0 = 5.94$ Å, 6.12 Å, and 6.46 Å for PbS, PbSe, and PbTe, respectively,²⁶ and they all have similar direct-gap semiconductor band structures. The constant energy surfaces for the conduction and valence bands of these lead salts are prolate ellipsoids of

revolution centered at the four equivalent L points in the Brillouin zone, and the major axes of these ellipsoids are in the $[111]$ directions.²⁶ There is a considerable band offset when combining two dissimilar lead salts together, and this band offset provides carrier confinement between quantum dots. The band structures of lead salts in bulk form have been studied extensively, and some of the important temperature-dependent parameters related to their transport properties are listed in Table II. To minimize the lattice mismatch at the heterogeneous interfaces, we choose to study PbS/PbSe and PbSe/PbTe superlattice nanowires in this paper, with particular emphasis on the PbS/PbSe systems. We note that the lattice mismatch may not be as significant an issue in superlattice nanowires as in superlattice thin films, since researchers have found that in superlattice nanowires, the lattice strain can be laterally relaxed to avoid defects at the interface.¹⁸

Based on the band-structure parameters in Table II, we first calculate the quantized subband energy ϵ_{nm} related to the confinement of the wire boundary in the x - y directions and the transport effective masses m_z along the wire axis. Since the carrier pockets of these lead salts are highly anisotropic, ϵ_{nm} and m_z are dependent on the crystallographic direction of the wire axis. For wires oriented along the $[001]$ direction, the four L pockets are all degenerate and are denoted as $L^{(4)}$; for wires oriented along the $[111]$ direction, this fourfold degeneracy is lifted, resulting in two inequivalent groups of carrier pockets: a single pocket with its major axis along the wire axis (denoted as $L^{(1)}$), and the other three pockets that are still degenerate in energy (denoted as $L^{(3)}$). The subband energy ϵ_{nm} , which is inversely proportional to d_w^2 , is calculated for the three lead salts at 77 K for two wire orientations ($[001]$ and $[111]$), and the results are listed in Tables III and IV for the first five subbands for the electrons and holes, respectively. The transport effective masses along the wire axis of the various lead salts and orientations are given in Table V. We note that since the $L^{(1)}$ carriers of these lead salts usually have their largest mass component along the wire axis and their smallest mass components in the quantum confined directions, they possess a

TABLE III. The first five subband energies ($\chi_{nm} \equiv \epsilon_{nm} d_w^2$) normalized to the wire diameter d_w and given in units of eV nm² for each distinct electron pocket in various lead salts and wire orientations at 77 K. The χ_{nm} values are listed in the order of increasing energy.

Material	Orientation	Pocket	Order =	1	2	3	4	5
PbS	[001]	$L_e^{(4)}$		9.52	23.17	25.14	42.49	43.48
	[111]	$L_e^{(1)}$		10.30	26.12	26.12	46.92	46.92
	[111]	$L_e^{(3)}$		9.26	22.19	24.80	40.69	42.19
PbSe	[001]	$L_e^{(4)}$		16.70	38.85	45.85	70.90	75.99
	[111]	$L_e^{(1)}$		19.47	49.40	49.40	88.72	88.72
	[111]	$L_e^{(3)}$		15.77	25.31	44.63	63.70	71.65
PbTe	[001]	$L_e^{(4)}$		25.32	50.79	77.38	87.37	114.35
	[111]	$L_e^{(1)}$		35.98	91.27	91.27	163.94	163.94
	[111]	$L_e^{(3)}$		21.61	36.85	57.79	72.11	84.65

larger subband energy and a heavier transport effective mass along the wire axis compared to other pockets.

The subband energy and the transport effective masses in each segment are the fundamental parameters in determining the subband offset [see Eq. (3)] and the subband dispersion relation $E_{nm}(\kappa)$ of the superlattice nanowires. Assuming an equal *bulk* band offset for the conduction and valence bands in a heterogeneous structure constructed from two lead salts and choosing the zero energy to be at the middle of the bulk band gap, the (n, m) subband edge energy of a segment made of material X (PbS, PbSe, or PbTe) is given by

$$E_{nm}^X = \pm \left(\frac{E_g^X}{2} + \frac{\chi_{nm}^X}{d_w^2} \right) \quad (30)$$

for electrons (+) and holes (−), where $\chi_{nm} = \epsilon_{nm} \cdot d_w^2$ is a diameter-independent parameter, with values given in Tables III and IV for electrons and holes, respectively.

It should be noted that the potential barrier and well regions of a *bulk* heterogeneous structure may be inverted in a superlattice nanowire due to this diameter-dependent subband energy ϵ_{nm} . For example, Fig. 3 shows the first subband edge energies of PbS, PbSe, and PbTe nanodots oriented in the [001] direction as a function of wire diameter at 77 K. In bulk form, the band-gap (E_g) relation of the three

lead salts is PbSe < PbTe < PbS, and hence PbSe constitutes the potential-well region for electrons in PbSe/PbS or PbSe/PbTe heterostructures, as depicted by the upper-right inset of Fig. 3. However, as the wire diameter decreases, the subband edge energy of PbS nanodots increases at a slower rate than that of PbSe or PbTe nanodots because of the heavier carrier effective masses in PbS, and the first subband energy of PbS nanodots crosses that of PbTe and PbSe at $d_w \sim 18$ and 10 nm, respectively. The insets in Fig. 3 sketch the relative energy levels of the first subband edge of these lead salts in three different diameter ranges, showing that for small-diameter superlattice nanowires (e.g., PbSe/PbS), some of the subbands in the nanowire may undergo a potential barrier–well inversion when the subband edge energies of PbS nanodots become lower than those of the corresponding PbSe subbands. Due to the carrier anisotropy of these lead salts, the critical wire diameter for the potential barrier–well inversion is also dependent on the crystallographic direction, and for the [111] orientation, the lowest-lying $L_e^{(3)}$ conduction subband of PbS crosses those of PbSe and PbTe at $d_w \sim 16$ and 10 nm, respectively. This subband edge crossing and barrier-well inversion induced by quantum confinement, which is absent in other systems, such as 2D superlattice thin films, are unique properties of superlattice nanowires, and they hold important implications for carrier transport phe-

TABLE IV. The first five subband energies ($\chi_{nm} \equiv \epsilon_{nm} d_w^2$) normalized to the wire diameter d_w and given in units of eV nm² for each distinct hole pocket in various lead salts and wire orientations at 77 K. The χ_{nm} values are listed in the order of increasing energy.

Material	Orientation	Pocket	Order =	1	2	3	4	5
PbS	[001]	$L_h^{(4)}$		9.99	24.07	26.62	44.14	45.51
	[111]	$L_h^{(1)}$		11.00	27.91	27.91	50.13	50.13
	[111]	$L_h^{(3)}$		9.65	22.78	26.19	41.70	43.95
PbSe	[001]	$L_h^{(4)}$		19.39	44.18	54.16	80.17	88.19
	[111]	$L_h^{(1)}$		23.35	59.24	59.24	106.40	106.40
	[111]	$L_h^{(3)}$		18.06	39.12	52.41	69.69	81.95
PbTe	[001]	$L_h^{(4)}$		22.46	44.71	68.97	76.61	101.39
	[111]	$L_h^{(1)}$		32.19	81.68	81.68	146.70	146.70
	[111]	$L_h^{(3)}$		19.06	31.94	49.54	64.11	72.03

TABLE V. Calculated transport effective masses along the wire axis for each carrier pocket in various lead salts with different wire orientations. All effective mass coefficients are normalized to the free electron mass.

Material	[100] Direction		[111] Direction			
	$m_{e,z}$	$m_{h,z}$	$m_{e,z}^{(1)}$	$m_{e,z}^{(3)}$	$m_{h,z}^{(1)}$	$m_{h,z}^{(3)}$
PbS	0.0939	0.0903	0.1105	0.0884	0.1105	0.0835
PbSe	0.0564	0.0506	0.0788	0.0490	0.0764	0.0421
PbTe	0.0829	0.1051	0.2000	0.0440	0.2607	0.0533

nomena. Since the theoretical formalism developed for superlattice nanowires in Sec. II treats the potential well A and barrier B symmetrically, the effect of this potential barrier-well inversion can be readily addressed in the following model calculations for lead salt superlattice nanowires. We note that since the band offset vanishes at the crossing of corresponding subbands of the two materials, the carriers in that subband may travel along the wire like free carriers without the potential barrier, which may be desirable for certain transport-related applications. It is also interesting to compare this potential-well inversion in superlattice nanowires to the semimetal-semiconductor transition observed in Bi nanowires,¹⁰ which results from the subband crossing due to a diameter-dependent phase diagram.

Figure 4 shows the calculated density of states of the conduction band for [001] PbSe/PbS superlattice nanowires as a function of energy at 77 K with a wire diameter of $d_w = 10$ nm and equal segment lengths $L_{\text{PbSe}} = L_{\text{PbS}} = 5$ nm. The density of states of PbS_{0.5}Se_{0.5} alloy nanowires with the same diameter and orientation is also plotted in Fig. 4 for comparison. We note that for alloy nanowires, the singularities in the

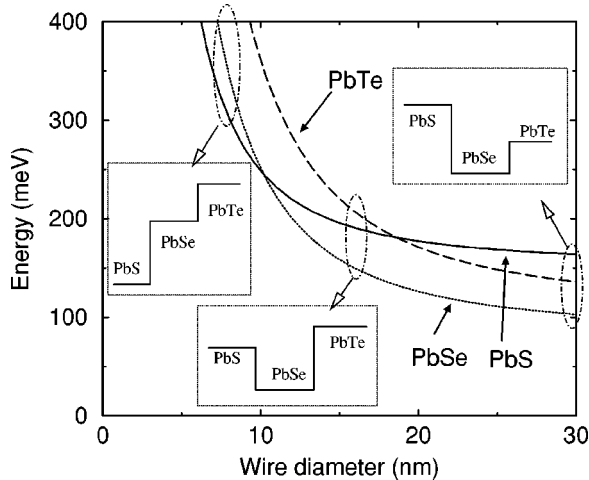


FIG. 3. The subband energy of various lead salt nanodots oriented in the [001] direction at 77 K, showing the first subband energy vs wire diameter. The zero energy refers to the middle of the bulk band gap. As d_w decreases, the subbands moves up in energy, and the PbS subband (—) crosses those of PbTe (- - -) and PbSe (· · ·) at $d_w \sim 18$ nm and 10 nm, respectively. The three insets depict the relation of the subband edge energies of the three lead salts in different diameter ranges.

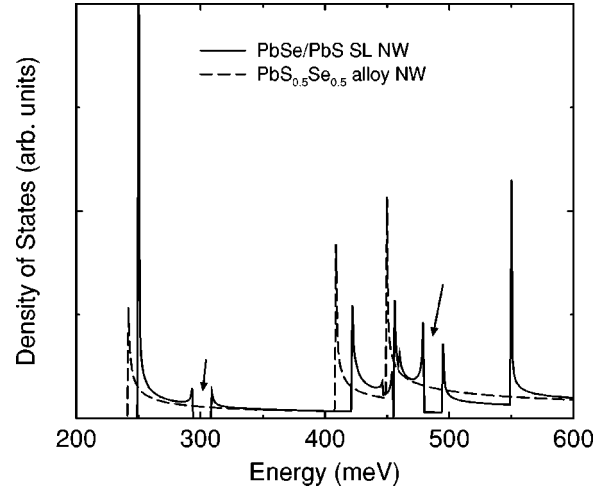


FIG. 4. Calculated density of states for [001] PbSe/PbS superlattice nanowires (—) with wire diameter $d_w = 10$ nm and segment lengths $L_{\text{PbSe}} = L_{\text{PbS}} = 5$ nm at 77 K. The arrows indicate the minigaps resulting from the periodic potential in the superlattice nanowires. It is noted that due to the superposition of multiple subbands, the minigap indicated by the second arrow at $E \sim 490$ meV has nonvanishing density of states. The calculated density of states for PbS_{0.5}Se_{0.5} nanowires (- - -) with the same wire diameter and orientation is also shown in the dashed curve for comparison.

electronic density of states correspond to individual 1D subband edges ϵ_{nm} , and for each subband the density of states varies as $(E - \epsilon_{nm})^{-1/2}$. In contrast, the density of states for superlattice nanowires usually exhibits a more complicated energy dependence with additional singularities resulting from the minigaps, as indicated by the arrows in Fig. 4. The superposition of multiple subbands further enriches the behavior of the density of states in superlattice nanowires, as those shown at $E \sim 450$ meV. It should also be pointed out that the density of states profile of these lead salt superlattice nanowires is highly sensitive to the crystal orientation because of their multiple anisotropic carrier pockets. These interesting features in the dispersion relation along the transport direction, which are absent in either simple nanowires or in 2D superlattice systems, are unique to superlattice nanowires, and they are responsible for some unusual transport properties predicted in the superlattice nanowires, as will be discussed in the following section.

B. Transport and thermoelectric properties

In this section, we calculate transport properties for superlattice nanowires composed of various lead salts, and we investigate their potential for thermoelectric applications, based on the electronic band structure model and the transport equations developed in previous sections. The thermoelectric performance is usually measured in terms of a dimensionless figure of merit ZT , defined as

$$ZT = \frac{S^2 \sigma}{\lambda} T, \quad (31)$$

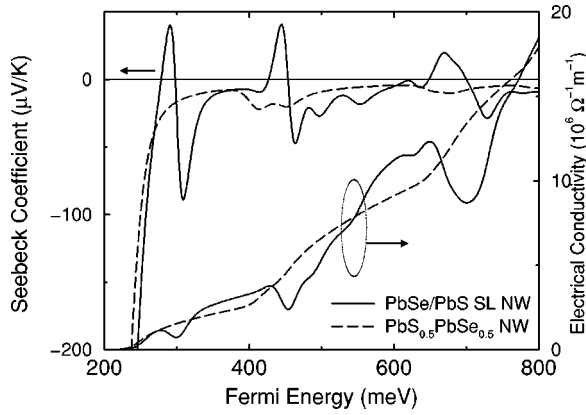


FIG. 5. Calculated Seebeck coefficient and electrical conductivity as a function of the Fermi energy for [001] PbSe (5 nm)/PbS (5 nm) superlattice nanowires (—) and PbS_{0.5}Se_{0.5} alloy nanowires (- - -) at 77 K. The diameters are $d_w = 10$ nm for both types of nanowires.

where S , σ , and λ are the Seebeck coefficient, electrical conductivity, and the thermal conductivity (including contributions from electrons and phonons), respectively.

Figure 5 shows the calculated Seebeck coefficient and electrical conductivity as a function of Fermi energy for [001] PbSe/PbS superlattice nanowires with a diameter $d_w = 10$ nm and segment lengths $L_{\text{PbS}} = L_{\text{PbSe}} = 5$ nm at 77 K, as well as the calculated results for PbS_{0.5}Se_{0.5} alloy nanowires with the same diameter and crystal orientation. The relaxation times τ of electrons and holes, required for calculating various transport-related integrals [see Eqs. (18) and (19)], are derived from the carrier mobility of bulk materials²⁷ using the relation $\mu = e\tau/m^*$, as listed in Table VI for various lead salts at 77 K. However, we note that the carrier mobility of low-dimensional systems may possess different values from those of their bulk counterparts. It is expected that μ may be lowered due to the extra scattering at the wire boundary and the heterogeneous interfaces, whereas the reduction in available final states for scattering events in low-dimensional systems may increase μ . Therefore, careful experimental studies are required to obtain a more accurate estimate for μ and to further improve model calculations.

As shown in Fig. 5, the electrical conductivity of a homogeneous (alloy) nanowire increases monotonically with increasing Fermi energy (or electron density), while that for the superlattice nanowires exhibits nonmonotonic variations, with local minima corresponding to the minigaps in the density of states (see Fig. 4). In Fig. 5, the Seebeck coefficient of superlattice nanowires also shows unusual behaviors due to

TABLE VI. Mobility of electrons and holes for various lead salts at 77 K (Ref. 27). The carrier relaxation time is derived using the relation $\tau = m\mu/e$.

Property, unit	PbS	PbSe	PbTe
μ_e (77 K), $\text{cm}^2 \text{V}^{-1} \text{s}^{-1}$	11000	16500	31600
μ_h (77 K), $\text{cm}^2 \text{V}^{-1} \text{s}^{-1}$	15000	13700	21600
τ_e (77 K), s	5.83×10^{-13}	5.11×10^{-13}	8.86×10^{-13}
τ_h (77 K), s	7.62×10^{-13}	3.73×10^{-13}	7.13×10^{-13}

the existence of the minigaps. We note that for alloy nanowires, the Seebeck coefficient is always negative, and the magnitude diminishes rapidly with increasing Fermi energy, except for some small fluctuations near the subband edges. Interestingly, for superlattice nanowires, the Seebeck coefficient not only shows strong oscillations near the minigaps, but it also becomes positive for certain energy ranges. This sign change in the Seebeck coefficient as the Fermi energy varies has important implications, indicating that the superlattice nanowires may be tailored to exhibit n - or p -type properties, using the same dopants (e.g., electron donors) by carefully controlling the Fermi energy or the dopant concentration. More importantly, we also note that the Seebeck coefficient extrema of superlattice nanowires have substantially larger magnitudes for Fermi energies near the minigaps with only slightly reduced electrical conductivity compared to alloy nanowires (see Fig. 5), which is a direct consequence of the unique potential profile in the transport direction. It is noted that a similar behavior of enhanced Seebeck coefficient due to miniband formation has also been predicted by Balandin and co-workers for 3D quantum dot array structures,¹³ showing the impact of the periodic potential perturbation on transport properties. These observations are significant because they not only illustrate one of the advantages of superlattice nanowires for thermoelectric applications, but they may also account for the enhanced Seebeck coefficient and power factor ($S^2\sigma$) measured in quantum dot array systems and reported by Harman *et al.*, since both systems have similar periodic potential structures in the direction of carrier transport.

In order to obtain the thermoelectric figure of merit for the superlattice nanowires, Eqs. (23)–(29) are employed to calculate the lattice thermal conductivity. The heat capacity and the sound velocity of these lead salts, which are essential parameters in determining the phonon mean free path (mfp) in bulk materials, are inferred from the Debye temperature θ_D using the Debye model for the phonon dispersion relations. Table VII lists the Debye temperature, lattice thermal resistivity $1/\lambda$, and the calculated phonon mean free paths Λ for various bulk lead salts at 77 K.

With the lattice thermal conductivities thus obtained, Fig. 6 shows the calculated ZT as a function of Fermi energy for [001] PbSe (5 nm)/PbS (5 nm) superlattice nanowires, and for the corresponding PbSe, PbS, and PbS_{0.5}Se_{0.5} alloy nanowires with diameters $d_w = 10$ nm at 77 K, showing an enhancement in ZT for superlattice nanowires over alloy or pure lead salt nanowires. At the appropriate placement of the Fermi energy, optimal ZT values of 0.65, 0.46, 0.36, and 0.22 are obtained for PbSe/PbS superlattice nanowires, PbS_{0.5}Se_{0.5} alloy, PbSe, and PbS nanowires, respectively. Compared to homogeneous nanowires, there are more pronounced ZT extrema as a function of Fermi energy for superlattice nanowires due to the unusual Seebeck coefficient features in superlattice nanowires discussed earlier (see Fig. 5). It is interesting to note that, in Fig. 6, the second ZT maximum for superlattice nanowires corresponds to a positive Seebeck coefficient, whereas the first and the third peaks have negative Seebeck coefficients. Since the sign of the Seebeck coefficient is critical in determining the direction of

TABLE VII. Selected thermal properties of bulk lead salts. The temperature dependence of the thermal resistivity is linearly interpolated from values in Ref. 28 below 300 K, and the phonon mfp is calculated using Eq. (26).

Property	PbS	PbSe	PbTe
Debye temperature (Ref. 28) θ_D	220 K	160 K	130 K
Thermal resistivity $1/\lambda$ ($\text{W}^{-1} \text{mK}$)	$\begin{cases} 17.9T & (T \leq 180 \text{ K}) \\ 13.4T & (T \geq 240 \text{ K}) \end{cases}$	$\begin{cases} 24.2T & (T \leq 160 \text{ K}) \\ 19.5T & (T \geq 200 \text{ K}) \end{cases}$	16.42T
Phonon mfp Λ (77 K)	14.5 nm	13.2 nm	25 nm

heat and current flows for thermoelectric devices, this sign should be carefully identified in determining the optimal ZT for the superlattice nanowires.

Figure 7 shows the optimal ZT for n -type 10-nm-diameter PbSe/PbS superlattice nanowires as a function of segment length ($L_{\text{PbSe}} = L_{\text{PbS}}$) for two crystal orientations ([001] and [111]) at 77 K. For comparison, the inset of Fig. 7 shows the optimal ZT for $\text{PbS}_{0.5}\text{Se}_{0.5}$ alloy nanowires calculated as a function of wire diameter at 77 K. At a diameter $d_w = 10$ nm, the optimal ZT values are 0.46 and 0.39 for [001] and [111] alloy nanowires, respectively. We note that for both the PbSe/PbS superlattice and $\text{PbS}_{0.5}\text{Se}_{0.5}$ alloy nanowires, the nanowires oriented along the [001] direction possess a slightly higher ZT than [111] wires, possibly due to a higher density of states and smaller transport effective masses for [001] wires resulting from the four degenerate carrier pockets. As indicated in Fig. 7, the thermoelectric performance of the 10-nm superlattice nanowires increases rapidly as the segment length decreases, with ZT values higher than those of the corresponding alloy nanowires for segment lengths ≤ 7 nm. However, it is also noted that for longer segment lengths ($L_{\text{PbSe}} = L_{\text{PbS}} > 7$ nm), these superlattice nanowires exhibit a lower ZT than alloy nanowires, which may be due to a lower lattice thermal conductivity in the alloy nanowires. It is interesting to note how the thermoelectric performance of these superlattice and alloy nano-

wires, which contain the same number of Pb, S, and Se atoms, can be tailored by controlling the spatial arrangement (alloy vs periodic segments) of these constituent species.

Figure 8 displays the optimal ZT for n -type 5-nm-diameter PbSe/PbS superlattice nanowires as a function of segment length ($L_{\text{PbSe}} = L_{\text{PbS}}$) for two crystal orientations at 77 K, showing an oscillatory ZT behavior as the segment length varies. For comparison, the ZT values for 5-nm-diameter $\text{PbS}_{0.5}\text{Se}_{0.5}$ alloy nanowires are calculated as 1.7 and 1.4 for the [001] and [111] orientations (see the inset of Fig. 7), respectively. These ZT oscillations, which are absent or insignificant in larger diameter superlattice nanowires (see Fig. 7), are due to the larger subband separation as the wire diameter decreases. For example, the inset of Fig. 8 depicts the density of states for a 5-nm-diameter PbSe (10 nm)/PbS (10 nm) superlattice nanowire oriented along the [001] direction, showing that only *one* subband contributes to the transport properties in the energy range of importance, since the onset of the second subband does not appear until $E > 1000$ meV. In contrast, the density of states of 10-nm-diameter PbSe/PbS superlattice nanowires (see Fig. 4) exhibits a much more complicated energy dependence due to the superposition of multiple subbands in the energy range of optimal ZT . Therefore, for small diameter superlattice

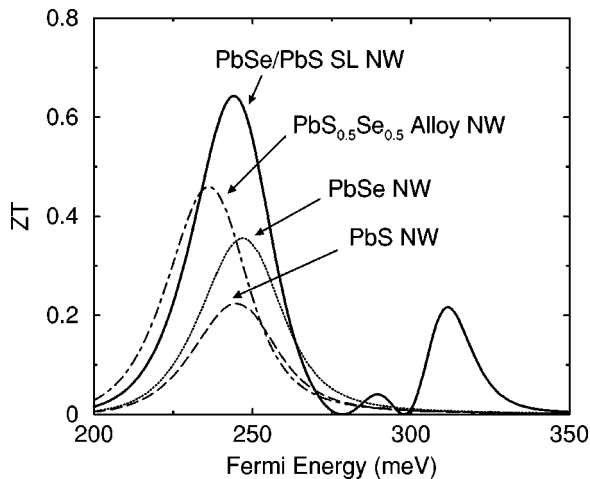


FIG. 6. Calculated ZT as a function of Fermi energy for [001] PbSe (5 nm)/PbS (5 nm) superlattice nanowires, as well as PbSe, PbS, and $\text{PbS}_{0.5}\text{Se}_{0.5}$ nanowires at 77 K. The wire diameters are 10 nm in all cases.

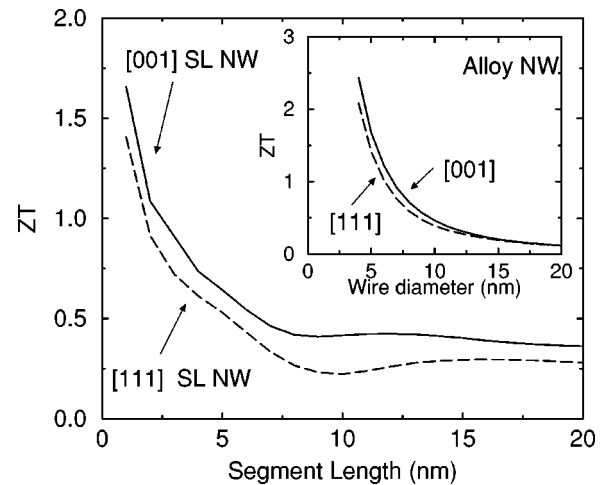


FIG. 7. Calculated optimal ZT as a function of the segment length for n -type 10-nm-diameter PbSe/PbS superlattice nanowires oriented along the [001] (—) and [111] (---) directions at 77 K. Inset: calculated ZT for $\text{PbS}_{0.5}\text{Se}_{0.5}$ nanowires oriented along the [001] (—) and [111] (---) directions as a function of the wire diameter at 77 K.

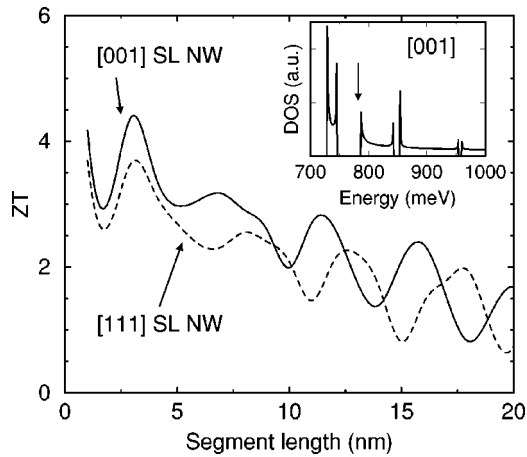


FIG. 8. Calculated optimal ZT of n -type 5-nm-diameter PbSe/PbS superlattice nanowires as a function of the segment length ($L_{\text{PbSe}}=L_{\text{PbS}}$) for [001] (—) and [111] (---) orientations at 77 K. Inset: electronic density of states of [001] PbSe/PbS superlattice nanowires with a wire diameter of 5 nm and $L_{\text{PbSe}}=L_{\text{PbS}}=10$ nm at 77 K. The arrow indicates the Fermi energy (~ 782 meV) where the optimal ZT occurs.

nanowires, their transport properties are mainly determined by the bandwidths of the minibands and the minigaps, which are highly dependent on the segment length, instead of the diameter-dependent subband energies. As shown in Fig. 2, the miniband and the minigap structure of one subband evolves from that of the *alloy* limit to the *classical* limit as the segment length increases, resulting in an oscillatory optimal ZT due to the variation in the widths and gaps of the minibands. However, for larger-diameter superlattice nanowires, this ZT oscillation as a function of segment length becomes smeared out due to the averaging effect of the contributions from multiple subbands. In Fig. 8, the optimal segment length for 5-nm-diameter PbSe/PbS superlattice nanowires is about 3 nm for both [001] and [111] orientations, with optimal ZT values of 4.4 and 3.7, respectively, which are much higher than the optimal ZT of 10-nm-diameter superlattice nanowires.

Since the lead salts have valence-band structures similar to their conduction bands, p -type lead salt superlattice nanowires are expected to exhibit similar thermoelectric performance in comparison to their n -type counterparts. Figure 9 calculates optimal ZT of p -type PbSe/PbS superlattice nanowires as a function of the segment length ($L_{\text{PbSe}}=L_{\text{PbS}}$) for two different wire diameters and crystal orientations, showing comparable ZT values and a similar dependence on the segment length to that for the n -type PbSe/PbS superlattice nanowires. The optimal ZT values for 5-nm-diameter p -type PbSe/PbS superlattice nanowires are calculated as 6.2 and 4.4 with segment lengths ~ 2 nm and ~ 3 nm for [001] and [111] orientations, respectively. We note that p -type PbSe/PbS superlattice nanowires have optimal ZT values, slightly higher than the n -type wires, which may be due to the smaller effective masses for holes than for electrons in PbSe and PbS (see Table V).

The thermoelectric performance of superlattice nanowires consisting of PbTe and PbSe segments is also calculated.

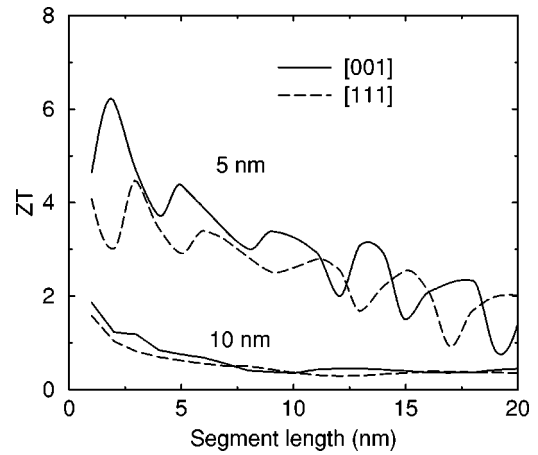


FIG. 9. Calculated optimal ZT of p -type PbSe/PbS superlattice nanowires as a function of the segment length ($L_{\text{PbSe}}=L_{\text{PbS}}$) for two different wire diameters oriented along [001] (—) and [111] (---) directions at 77 K.

Figure 10 shows the optimal ZT of n -type PbSe/PbTe superlattice nanowires as a function of segment length ($L_{\text{PbSe}}=L_{\text{PbTe}}$) for different diameters (5 nm and 10 nm) and crystal orientations ([001] and [111]) at 77 K. As indicated by Fig. 3, PbTe nanodots always constitute the potential barrier region in PbTe/PbSe superlattice nanowires, regardless of the wire diameter. We note that, in addition to the 5-nm-diameter nanowires, the oscillatory ZT behavior, although weaker, is also observed in the 10-nm PbSe/PbTe superlattice nanowires because of smaller effective masses and larger subband separations for PbTe. The optimal segment lengths for 5-nm-diameter PbTe/PbSe superlattice nanowires are both about 2 nm for [001] and [111] orientations, with optimal ZT values of 6.4 and 8.1, respectively. Compared with the results for PbSe/PbS superlattice nanowires in Fig. 7, we note that the PbSe/PbTe superlattice nanowires usually possess better thermoelectric performance than their PbSe/PbS counterparts, which may be due to the better thermoelectric proper-

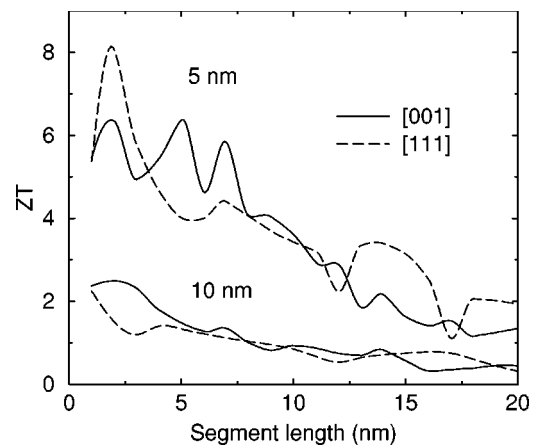


FIG. 10. Calculated optimal ZT of n -type PbSe/PbTe superlattice nanowires as a function of the segment length ($L_{\text{PbSe}}=L_{\text{PbTe}}$) for two different wire diameters (5 and 10 nm) oriented along the [001] (—) and [111] (---) directions at 77 K.

TABLE VIII. Optimal segment lengths and the highest ZT of 5-nm-diameter n - and p -type lead salt superlattice nanowires (PbSe/PbS and PbSe/PbTe) at 77 K.

Material Orientation		PbSe/PbS SLNW		PbSe/PbTe SLNW	
		[001]	[111]	[001]	[111]
n type	Optimal ZT	4.4	3.7	6.4	8.1
	Segment length	3 nm	3 nm	2 nm	2 nm
p type	Optimal ZT	6.2	4.4	6.0	7.6
	Segment length	2 nm	2 nm	2 nm	2 nm

ties for PbTe than for PbS in bulk form. In addition, the higher carrier anisotropy and smaller effective masses in PbTe than in PbS (see Tables II and V), which provide a larger density of states and lighter transport effective masses in nanowires, may also account for the higher ZT observed in PbTe/PbSe superlattice nanowires. Table VIII summarized the optimal ZT (n and p types) and the corresponding segment lengths for PbSe/PbS and PbSe/PbTe superlattice nanowires at 77 K. We notice that p -type PbSe/PbTe superlattice nanowires possess a lower ZT than their n -type counterparts, in contrast to the case of PbSe/PbS superlattice nanowires, which may result from the larger effective masses and lower mobilities for holes than for electrons in PbTe (see Tables II and VI).

The calculations shown so far are made assuming an equal segment length for the two constituent materials. However, for a given period length $L = L_A + L_B$ for superlattice nanowires, the thermoelectric performance may be further optimized by adjusting the length ratio of the two materials. As an example, Fig. 11 shows the calculated ZT for 5-nm-diameter n -type PbSe/PbS superlattice nanowires as a function of the PbSe segment length L_{PbSe} at a given period, $L = L_{\text{PbSe}} + L_{\text{PbS}} = 10$ nm, along two crystal orientations at 77

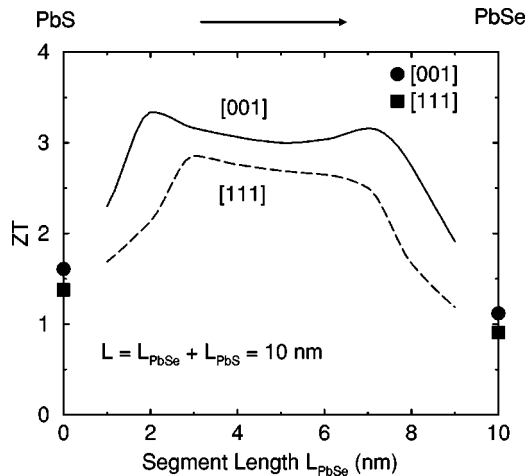


FIG. 11. Calculated optimal ZT for 5-nm-diameter n -type PbSe/PbS superlattice nanowires as a function of the PbSe segment length L_{PbSe} at 77 K with different nanowire crystalline orientations. The segment length of PbS is chosen such that the period $L = L_{\text{PbSe}} + L_{\text{PbS}}$ is constant and equals to 10 nm. The optimal ZT for 5-nm-diameter PbS and PbSe nanowires is shown as circles and squares for [001] and [111] orientations, respectively.

K. The optimal ZT of 5-nm-diameter PbSe and PbS nanowires at 77 K are also shown in Fig. 11 for [001] and [111] orientations as circles and squares, respectively. From Fig. 11, we see that a higher ZT can be achieved for PbSe/PbS superlattice nanowires with unequal segment lengths for PbSe and PbS nanodots. For [001] orientations, PbSe (2 nm)/PbS (8 nm) superlattice nanowires have the highest ZT of 3.3, while PbSe (3 nm)/PbS (7 nm) superlattice nanowires are optimal for the [111] orientation with $ZT \sim 2.8$. As a comparison, for $L_{\text{PbSe}} = L_{\text{PbS}} = 5$ nm, the optimal ZT values of corresponding [001] and [111] superlattice nanowires are calculated as 3.0 and 2.7, respectively. We note that since the electronic band structure and the lattice thermal conductivity of superlattice nanowires are highly dependent on the wire diameter, segment lengths, and the transport properties of their constituent materials, this optimal length ratio for the two components is not universal and may vary for different period lengths and wire diameters. Physically speaking, superlattice nanowires with unequal segment lengths may possess better thermoelectric properties than the ones with equal segment lengths because the thermal resistivity and/or thermopower can be maximized by increasing the length of materials with desirable attributes without losing the advantage of the superlattice structure.

According to Table VIII, we found that the optimal ZT is usually achieved for segment lengths as short as 2 nm for lead salt superlattice nanowires at a diameter of 5 nm. However, it is necessary to check these length scales for internal consistency with the model assumption. First, since the lattice constants of these lead salts are about 5 Å, there are ~ 400 unit cells in a nanodot with a diameter of 5 nm and segment length of 2 nm, validating the application of the effective mass theorem and the band-structure parameters used in the model calculation. In addition, the ζ values defined in Eq. (16) are calculated as ~ 0.4 and 0.5 , respectively, for the first subband of 5-nm-diameter [001] PbSe (2 nm)/PbS (2 nm) and PbSe (2 nm)/PbTe (2 nm) superlattice nanowires. Based on the criteria ($\zeta \leq 0.1$) for the alloy limit from previous discussions, these superlattice nanowires are not in the alloy limit, and they do possess a unique electronic band structure that is dramatically different from that for a simple nanowire, and this unique band structure partly accounts for their superior performance when compared to their corresponding alloy nanowires. Recently, Bjork and co-workers have fabricated InP/InAs superlattice nanowires with atomically perfect interfaces by chemical beam epitaxy¹⁸ for segment lengths as short as 1.5 nm, indicating that the proposed superlattice nanowire structures that are here discussed for thermoelectric applications may be achieved experimentally. Experimental studies of these nanowires, especially their carrier mobility, carrier concentration, and the interface and wire boundary conditions, are important in order to check the validity of the assumptions made in model calculations, such as are given here, and to further improve the values of the parameters used in such model predictions.

IV. CONCLUSIONS

In this paper, we present a model for superlattice nanowires to calculate their electronic band structure and trans-

port properties. The model considers the quantum confinement effects due to a cylindrical wire boundary and the formation of 1D subbands of anisotropic carriers. The dispersion relation of each subband in the superlattice nanowire is derived using the Kronig-Penney potential model, and exhibits very different features depending on the segment length. It is found that the electronic band structure of superlattice nanowires of very short and very long segment lengths can be well approximated by the superpositions of simple 1D band structures to substantially reduce the required computational complexity.

The thermoelectric properties of superlattice nanowires made of various lead salts (PbS, PbSe, and PbTe) are investigated based on the electronic band structure model described above and on the 1D Boltzmann transport equations. Due to the electron mass differences between different materials, the potential barrier-well inversion induced by quantum confinement, which is a unique phenomenon in superlattice nanowires, is observed as the wire diameter decreases. The thermoelectric figure of merit, ZT , of these superlattice nanowires is found to be highly dependent on the segment length, wire diameter, crystal orientation, selection of material constituents, Fermi energy, and the segment length ratio. It is found that ZT generally increases with decreasing wire diameter and with decreasing segment length before the alloy limit is reached. As a general guidance for thermoelectric applications, it is usually desirable to design superlattice nanowires composed of materials that have (1) semiconducting band structures, (2) low interdiffusion at the interface for effective carrier confinement to occur, and (3) multiple carrier pockets with high anisotropy to achieve a large density of states and small transport effective masses simultaneously.

For PbSe/PbS superlattice nanowires, ZT values higher than those of $\text{PbS}_{0.5}\text{Se}_{0.5}$ alloy nanowires are possible for segment lengths L_{PbS} and L_{PbSe} smaller than ~ 10 nm, with an optimal $ZT > 4$ for 5-nm-diameter PbSe/PbS superlattice nanowires. PbTe/PbSe superlattice nanowires are expected to possess even better thermoelectric performance than the cor-

responding PbSe/PbS systems with values as high as $ZT > 6$ for optimal doping because of a larger carrier anisotropy and smaller effective masses in PbTe. The results indicate that superlattice nanowires are promising systems for thermoelectric applications, when the nanowires are properly doped and designed. For the lead salt superlattice nanowires studied here, it is necessary to choose segment lengths smaller than the wire diameter in order to have higher ZT values than for their corresponding alloy nanowires, and for 5-nm-diameter superlattice nanowires, the optimal segment length is $\sim 2-3$ nm. For a given superlattice period, model calculations show that the ZT can be further improved by adopting different segment lengths for the two constituent materials. The model developed here not only makes predictions for the optimal parameters (segment length, diameter, materials, and doping level) for thermoelectric applications, but it can also be extended to other superlattice systems, such as 3D quantum dot arrays. Furthermore, the theoretical foundation given here also provides a general framework to study properties of interest for other applications of superlattice nanowires. It should be noted that, although the results derived from the theoretical calculations are found to be self-consistent with the model assumptions, transport measurements on realistic superlattice nanowires, which, to the authors' knowledge, are not currently available, would provide valuable information to verify the important approximations and predictions (e.g., the Kronig-Penney potential for subbands and the potential barrier-well inversion), and to further improve the theoretical model.

ACKNOWLEDGMENTS

The authors thank Dr. G. Dresselhaus, Dr. J. Heremans, O. Rabin, and M. R. Black for valuable comments on the band structure calculations. They are also grateful to Professor G. Chen and C. Dames for inspiring discussions on the thermal conductivity issues. The support from the DARPA-HERETIC/Caltech-JPL Contract No. 1237157 and the ONR Grant No. N00014-02-1-0865 is gratefully acknowledged.

*Email address: millie@mgm.mit.edu

¹M.S. Gudiksen, J.F. Wang, and C.M. Lieber, *J. Phys. Chem. B* **106**, 4036 (2002).

²X.F. Duan, Y. Huang, Y. Cui, J.F. Wang, and C.M. Lieber, *Nature (London)* **409**, 66 (2001).

³Y. Huang, X. Duan, Y. Cui, L.J. Lauhon, K.-H. Kim, and C.M. Lieber, *Science* **294**, 1313 (2001).

⁴T.C. Harman, P.J. Taylor, M.P. Walsh, and B.E. LaForge, *Science* **297**, 2229 (2002).

⁵Y.-M. Lin, O. Rabin, S.B. Cronin, J.Y. Ying, and M.S. Dresselhaus, *Appl. Phys. Lett.* **81**, 2403 (2002).

⁶R. Venkatasubramanian, E. Siivola, T. Colpitts, and B. O'Quinn, *Nature (London)* **413**, 597 (2001).

⁷K. Nielsch, R.B. Wehrspohn, J. Barthel, U. Gosele, S.F. Fischer, and H. Kronmüller, *Appl. Phys. Lett.* **79**, 1360 (2001).

⁸L.D. Hicks and M.S. Dresselhaus, *Phys. Rev. B* **47**, 12 727 (1993).

⁹L.D. Hicks and M.S. Dresselhaus, *Phys. Rev. B* **47**, 16 631 (1993).

¹⁰Y.-M. Lin, X. Sun, and M.S. Dresselhaus, *Phys. Rev. B* **62**, 4610 (2000).

¹¹M.S. Dresselhaus, Y.-M. Lin, T. Koga, S.B. Cronin, O. Rabin, M.R. Black, and G. Dresselhaus, in *Semiconductors and Semimetals: Recent Trends in Thermoelectric Materials Research III*, edited by T.M. Tritt (Academic, San Diego, CA, 2001), Chap. 1.

¹²L. Piraux, I.M. George, J.F. Despres, C. Leroy, E. Ferain, R. Legras, K. Ounadjela, and A. Fert, *Appl. Phys. Lett.* **65**, 2484 (1994).

¹³A.A. Balandin and O.L. Lazarenkova, *Appl. Phys. Lett.* **82**, 415 (2003).

¹⁴C. Dames and G. Chen, *J. Appl. Phys.* (submitted).

¹⁵Y. Wu, R. Fan, and P. Yang, *Nano Lett.* **2**, 83 (2002).

¹⁶M.S. Gudiksen, L.J. Lauhon, J. Wang, D.C. Smith, and C.M. Lieber, *Nature (London)* **415**, 617 (2002).

¹⁷M.T. Bjork, B.J. Ohlsson, C. Thelander, A.I. Persson, K. Deppert, L.R. Wallenberg, and L. Samuelson, *Appl. Phys. Lett.* **81**, 4458 (2002).

¹⁸M.T. Bjork, B.J. Ohlsson, T. Sass, A.I. Persson, C. Thelander,

- M.H. Magnusson, K. Deppert, L.R. Wallenberg, and L. Samuelson, *Nano Lett.* **2**, 87 (2002).
- ¹⁹N.W. Ashcroft and N.D. Mermin, in *Solid State Physics* (Holt, Rinehart and Winston, New York, 1976), Chap. 8.
- ²⁰C. Kittel, *Introduction to Solid State Physics*, 7th ed. (Wiley, New York, 1996), p. 180.
- ²¹The energy separation between minibands in the potential well is estimated by $\epsilon_g \sim V_b/n$, where V_b is the potential barrier height and n is the number of confined states in the potential well. To the first-order approximation, we calculate n by setting $E_n = V_b$, where $E_n = n^2 \pi^2 \hbar^2 / 2mL^2$ is the energy of the n th quantized state in an infinite potential well.
- ²²G. Chen, *Phys. Rev. B* **57**, 14 958 (1998).
- ²³E.T Swartz and R.O. Pohl, *Rev. Mod. Phys.* **61**, 605 (1989).
- ²⁴H. Preier, *Appl. Phys.* **20**, 189 (1979).
- ²⁵A.F. Ioffe, *Semiconductor Thermoelectric and Thermoelectric Cooling* (Infosearch, London, 1957).
- ²⁶R. Dalven, *Infrared Phys.* **9**, 141 (1969).
- ²⁷R.S. Allgaier and W.W. Scanlon, *Phys. Rev.* **111**, 1029 (1958).
- ²⁸Yu. I. Ravich, B.A. Efimova, and I.A. Smirnov, in *Semiconducting Lead Chalcogenides*, edited by L.S. Stil'bans (Plenum, New York, 1970), Chap. 4.